

Topological signatures of collective dynamics and turbulent-like energy cascades in active granular matter

Zihan Zheng^{1,2}, Cunyuan Jiang^{1,3,4}, Yangrui Chen^{1,2}, Matteo Baggioli^{1,3,4},* and Jie Zhang^{1,2}†

¹*School of Physics and Astronomy, Shanghai Jiao Tong University, Shanghai 200240, China*

²*Institute of Natural Sciences, Shanghai Jiao Tong University, Shanghai 200240, China*

³*Wilczek Quantum Center, School of Physics and Astronomy, Shanghai Jiao Tong University, Shanghai 200240, China and*

⁴*Shanghai Research Center for Quantum Sciences, Shanghai 201315, China*

(Dated: April 4, 2025)

Active matter refers to a broad class of non-equilibrium systems where energy is continuously injected at the level of individual “particles.” These systems exhibit emergent collective behaviors that have no direct thermal-equilibrium counterpart. Their scale ranges from micrometer-sized swarms of bacteria to meter-scale human crowds. In recent years, the role of topology and self-propelled topological defects in active systems has garnered significant attention, particularly in polar and nematic active matter. Building on these ideas, we investigate emergent collective dynamics in apolar active granular fluids. Using granular vibrators as a model experimental system of apolar active Brownian particles in a dry environment, we uncover a distinctive three-stage time evolution arising from the intricate interplay between activity and inelastic interactions. By analyzing the statistics, spatial correlations, and dynamics of vortex-like topological defects in the displacement vector field, we demonstrate their ability to describe and predict this intrinsic collective motion. Furthermore, we show that topological defects play a crucial role in the development of a turbulent-like inverse energy cascade, where kinetic energy transfers across different length scales over time. As the system evolves, the power scaling of the energy transfer increases with the duration of observation. Our findings demonstrate how topological concepts can be applied to predict macroscopic collective phenomena in apolar active matter. This establishes a direct link between microscopic topological dynamics and large-scale behaviors in active granular fluids.

INTRODUCTION

Living and nonliving out-of-equilibrium systems in which the motion of the individual constituents is propelled by an energy input that acts individually and independently on each of them are broadly classified under the common umbrella of *active matter*. Research in this field has expanded so rapidly in recent years that it now requires “a review of reviews” [1]. Active matter spans an extensive range of scales and appears in a wide class of systems from the bats in *Batman Returns* movie [2] to human crowds partying during traditional celebrations [3].

Activity inherently disrupts energy conservation and detailed balance, challenging fundamental principles of thermodynamics and statistical physics [4]. Moreover, the interplay between activity and intrinsic interactions in active systems leads to novel non-equilibrium phases of matter, characterized by emergent collective dynamics and spontaneous spatiotemporal patterns [5].

In contrast to living systems, granular materials are often considered outside the realm of active substances. Granular matter consists of numerous grains, typically larger than $100\ \mu\text{m}$, where thermal fluctuations are negligible [6–8]. A pile of sand serves as a prototypical example. Over the past several decades, extensive research

has explored the unique properties of granular matter as an athermal amorphous solid, focusing on various fundamental aspects. Key areas of study include packing properties [9, 10], granular statistical mechanics [11–13], jamming transitions and their associated marginal features [14–23], and inhomogeneous internal stress transmission [24–27]. Although inherently athermal, granular systems display complex rheological and mechanical properties when subjected to external driving forces, such as shear [28–33].

More recently, activity has been introduced into quasi-two-dimensional granular systems by placing a layer of granular particles on a vibrating surface, effectively supplying energy to individual particles and allowing them to behave as self-propelling units. A wide range of intriguing phenomena has been observed in these systems, including large-scale collective motion in vibrated polar disks [34] and tapered rods [35], giant number density fluctuations in swarming granular rods [36], dispersionless vibrational modes [37] and gapped shear waves [38] in bidisperse nonpolar Brownian vibrators, as well as high-energy velocity tails in granular spinners [39] and monodisperse nonpolar Brownian vibrators [40]. Additionally, flocking behavior has been observed in monodisperse nonpolar Brownian vibrators [41]. These systems, commonly referred to as *active granular matter*, form the central focus of our work.

Topology has emerged as a powerful tool for characterizing active media, with applications spanning phase transition, material design and biological systems [42–

* Corresponding Author: b.matteo@sjtu.edu.cn

† Corresponding Author: jiezhang2012@sjtu.edu.cn

50]. In particular, topological defects provide a framework for understanding collective dynamics and relaxation mechanisms in active systems [51–53]. Much of this research has focused on active polar fluids and nematics [54], revealing striking analogies with non-Hermitian condensed matter systems [55, 56] and offering new perspectives on active fluid behavior. In such fluids, topological defects act as quasiparticles driven by internal active stresses, generating chaotic flows and turbulence [52, 57–64]. Beyond active turbulence, defects can be manipulated to perform computations and transmit information, suggesting novel applications in active matter research [65–69].

Historically, topology has played a central role in studying polar and nematic active systems, where anisotropic shapes or directional self-propulsion define preferred orientations. Familiar concepts from liquid crystals [70] apply directly in these contexts. Collective motion, typically associated with self-aligning interactions—as exemplified by the Vicsek model [71]—was long thought to be restricted to such systems. However, recent theoretical work [72], later confirmed experimentally [41], demonstrated that flocking and large-scale motion can also arise in active granular systems without self-aligning interactions. In these systems, effective attractive forces emerge from inelastic collisions, driving collective behavior.

This work aims to extend the role of topology in non-polar active granular systems without self-aligning interactions, proving a direct connection between topological defect dynamics, large-scale collective motion, and turbulent-like structures.

ACTIVE GRANULAR FLUIDS

In Figure 1, we present the most salient features of our experimental setup and the essential ingredients to understand the underlying physics.

The microscopic constituents in our experimental platform are active Brownian particles that were 3D printed using a resin material. Each particle consists of a disk-shaped cap with 12 staggered legs attached underneath, as shown in Fig. 1(a). We utilize bidisperse particles with radii of $R_l = 11.2$ mm for large particles and $R_s = 8$ mm for small particles. The other geometric characteristics are the same for large and small particles, namely disk thickness ($h_1 = 3$ mm), leg height ($h_2 = 3$ mm), and placement of 12 staggered legs along a concentric circle of radius $r = 5.6$ mm. The mixing ratio between large and small particles is 1 : 2. Given their size ratio ($R_l : R_s = 1.4 : 1$), the total area occupied by large and small particles remains equal, maintaining a 1 : 1 area ratio in the whole system.

A single layer of particles is then placed on an aluminum plate within a flower-shaped region mounted on top of an electromagnetic shaker, see Figure 1(b). The electromagnetic shaker generates a vertical sinusoidal vi-

bration at 100 Hz, driving the entire system at the individual particle level with a maximum acceleration of $2.5g$, where g is the gravitational acceleration. A Basler CCD camera (not shown in the image) is positioned above the experimental platform and continuously records particle configurations for an hour at a rate of 40 frames per second. Figure 1(d, f) provides two images of the particles captured by the camera at different packing fractions.

During an experimental run, each particle individually receives kinetic energy from the shaker’s vertical vibration and dissipates it through collisions with other particles and with the plate mounted on the shaker. Once the energy injection and the dissipation balance on average, a non-equilibrium steady state is reached. The system’s complex dynamics and collective motions arise from the interplay between individual particle activity and interparticle inelastic interactions, as illustrated in the schematic representations in Fig.1(c) and (e).

The competition between these effects gives rise to two distinct dynamical behaviors, observed at low and high packing fractions (panels (d) and (f) in the same Figure). The packing fraction is defined as the ratio of the area occupied by the particles to the total area of the system. At low packing fractions, activity is dominant. Fig.1(d) shows the random displacement field superimposed on the individual particles within this regime, at a low packing fraction $\phi = 0.309$. Due to the unique leg design, a single particle gains kinetic energy through stochastic collisions between its legs and the bottom plate, resulting in random walk motion along the two-dimensional horizontal plane. This mechanism acts independently on each particle, giving rise to random gas-like motion as illustrated in Fig.1(c).

In this dilute limit, the dynamics are uncorrelated, and a single particle’s translational and rotational motions follow Gaussian distributions with zero mean, as demonstrated in previous studies [40]. Thus, these particles can be considered a granular realization of *active Brownian particles* [73]. On the other hand, as shown in Fig.1(e), inelastic interactions tend to correlate the dynamics of the individual particles, leading to collective motion involving clusters of neighbor particles. This effect becomes more pronounced by increasing the packing fraction. In the sufficiently dense regime, particle-particle interactions dominate over individual particle activity, giving rise to collective motion. At a high packing fraction ($\phi = 0.822$), large collective structures, with vortex-like form, appear in the particle displacement field, as illustrated in Fig.1(f).

In summary, the competition between activity and inelastic interactions appears to be the physical mechanism behind the emergence of a gas-like to liquid-like crossover upon increase the packing fraction [38].

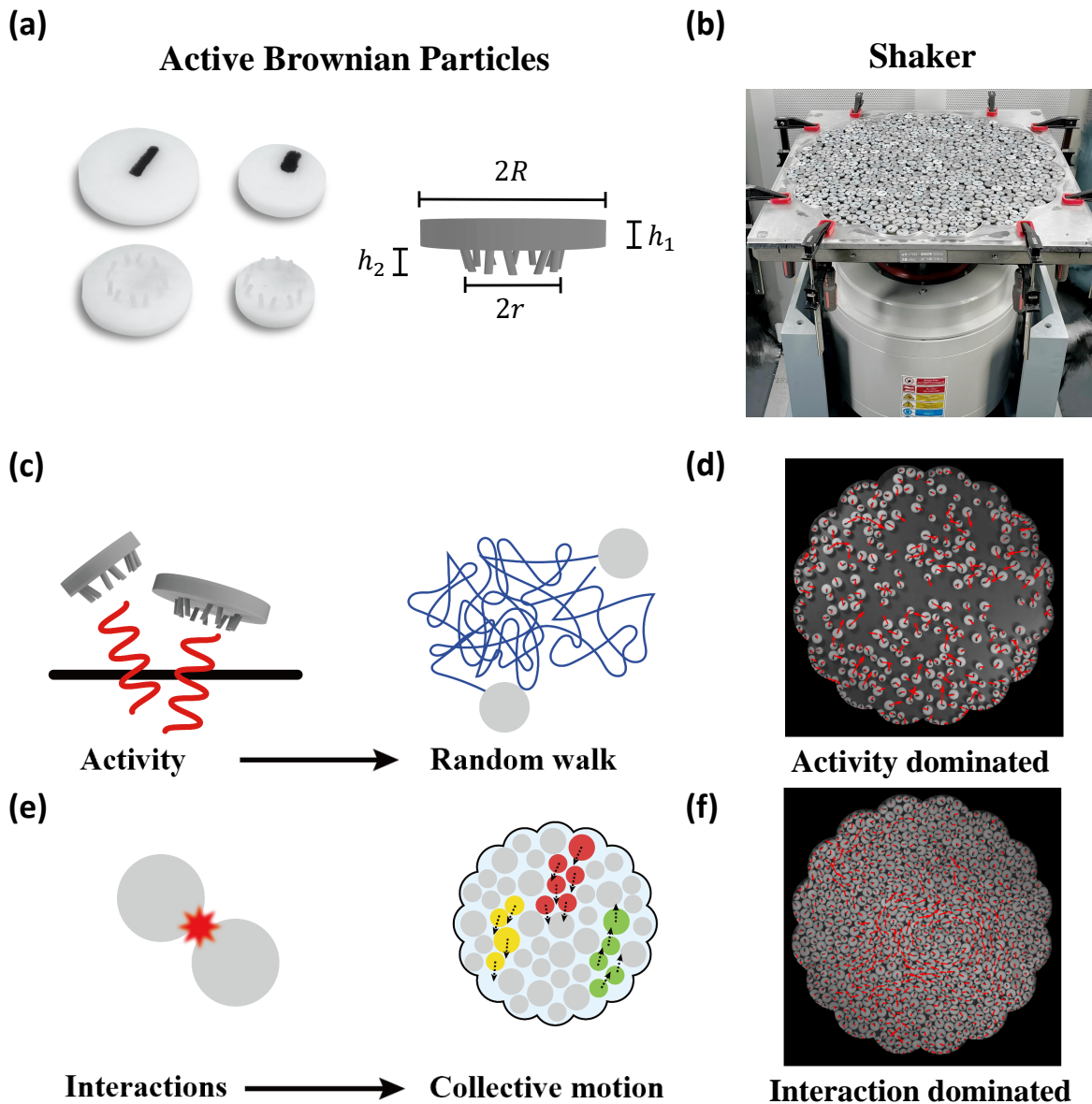


FIG. 1. **Experimental setup and underlying physics.** (a) Images of the large and small active Brownian particles used in our experiment. *Left:* Photos showing the top and bottom views of both particle types. *Right:* A schematic diagram illustrating the particle structure with relevant dimensions. (b) An image of the electromagnetic shaker, with a layer of bi-disperse particles placed on an aluminum plate mounted on the shaker. (c) When subjected to vertical vibrations, particles gain kinetic energy individually. This activity induces random collisions, primarily between one of their legs and the bottom plate, leading to isotropic random walk motion in the horizontal 2D plane. (d) Displacement vector field of bi-disperse particles at a low packing fraction ($\phi = 0.309$), where activity dominates leading to uncorrelated gas-like dynamics. (e) A schematic diagram illustrating how collective dynamics emerge from particle-particle inelastic interactions that become dominant at high packing fractions. (f) Displacement field of bi-disperse particles at a high packing fraction ($\phi = 0.822$), exhibiting collective vortex-like structures driven by interparticle interactions.

SELF-ORGANIZATION AND ONSET OF COLLECTIVE MOTION

To facilitate the computation of relevant physical quantities characterizing self-organization and collective motion, we first discretize the raw particle displacement

fields (such as those shown in Fig. 1(d,f)) by mapping them onto square lattice of size $1.84 D_s$. More precisely, a raw displacement field is defined as $\mathbf{u}_i \equiv \mathbf{r}_i(t_0 + \tau) - \mathbf{r}_i(t_0)$, where $\mathbf{r}_i(t)$ denotes the position of particle i at time t . Here, i indexes the particles, t_0 represents a specific reference time, and τ is the duration of observation time.

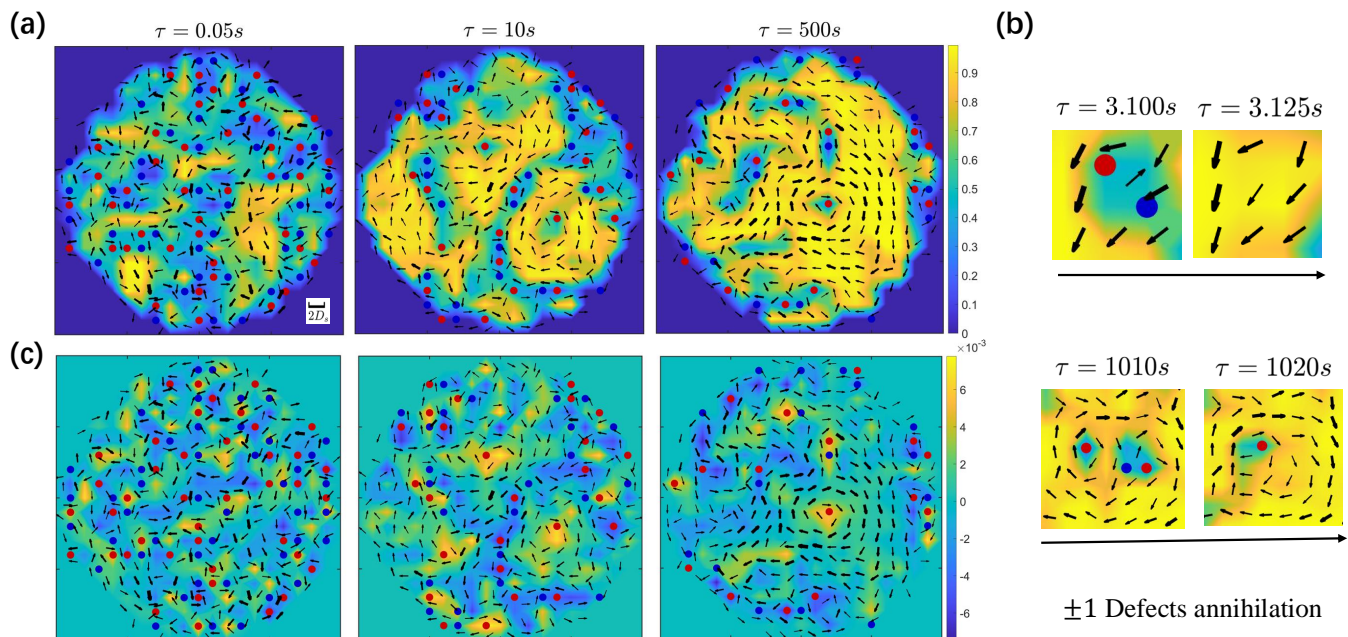


FIG. 2. **Topological defects characterize the self-organization and the onset of collective motion.** (a) Displacement field (black arrows with thickness representing magnitude) for different observation times, $\tau = 0.05s$, $10s$ and $500s$. Red and blue symbols refer to vortices and anti-vortices with ± 1 winding number q . The color map represents the local value of the polarization P_c . As a reference, the white bar shows the length-scale $2D_s$, with D_s the diameter of the small particles. (b) Snapshots of two consecutive displacement frames highlighting the annihilation of a $+1$ vortex (red) with a -1 anti-vortex (blue), conserving the total topological charge q_{tot} (0 in the top panel and $+1$ in the bottom one). (c) Same representation as in panel (a) but with the color map indicating the local value of the vorticity intensity Ω_l .

To quantify the spontaneous emergence of collective behavior and the emergence of self-organizing large structures, we define the local displacement polarization

$$P_c = \frac{1}{n} \left| \sum_{l=1}^n \frac{\mathbf{u}_l}{|\mathbf{u}_l|} \right|, \quad (1)$$

where \mathbf{u}_l stands for the local displacement vector on a given lattice site $l = 1, 2, \dots, n$ with $n = 4$ for the chosen square lattice.

By construction, the parameter P_c goes from 0 , when particle displacements are random and uncorrelated, to 1 , when all displacements point locally toward the same direction. In a sense, P_c quantifies the degree of local flocking in the particle dynamics. If n is taken to be the total number of particle $n = N$, then P_c describes the onset of global flocking as usually employed in polar active systems, *e.g.*, Vicsek model [71].

To provide a further probe of collective behavior, we also introduce the intensity of the local curl of the displacement field,

$$\Omega_l = |\nabla \times \mathbf{u}_l| = |\partial_x u_{l,y} - \partial_y u_{l,x}|, \quad (2)$$

where \mathbf{u}_l represents the local displacement vector on a given lattice site. Ω_l is a measure of local displacement curl. A large value of Ω_l indicates a significant degree of local rotation in the displacement vector, which acts

in direct opposition to the polarization P_c . Heuristically, one would expect P_c and Ω_l to create a complementary network. This combination offers a more robust characterization of the onset of collective behavior at a local scale.

Finally, we analyze the local structure of the displacement vector field \mathbf{u}_l by looking for its singularities in the form of vortices and anti-vortices, *i.e.*, topological defects in the dynamical displacement field. In this respect, we define the topological winding number:

$$q \equiv \frac{1}{2\pi} \oint_C d\theta, \quad (3)$$

where θ is the direction (phase) of the local displacement vector concerning the x -axes and C a closed loop. $q = \pm 1$ corresponds respectively to a vortex/anti-vortex where the phase of the displacement vector is not well-defined, and the vector itself is singular. q is a topological conserved charge, insensitive to continuous transformations of the displacement field. It follows that, in a freely evolving system, a vortex can disappear only through annihilation with a corresponding anti-vortex, conserving the total topological charge of the system.

In Fig. 2, we present three snapshots of the particle displacements on the square lattice for three different observation times: $\tau = 0.05s$, $\tau = 10s$, and $\tau = 500s$. The local displacement vectors are visualized with black arrows

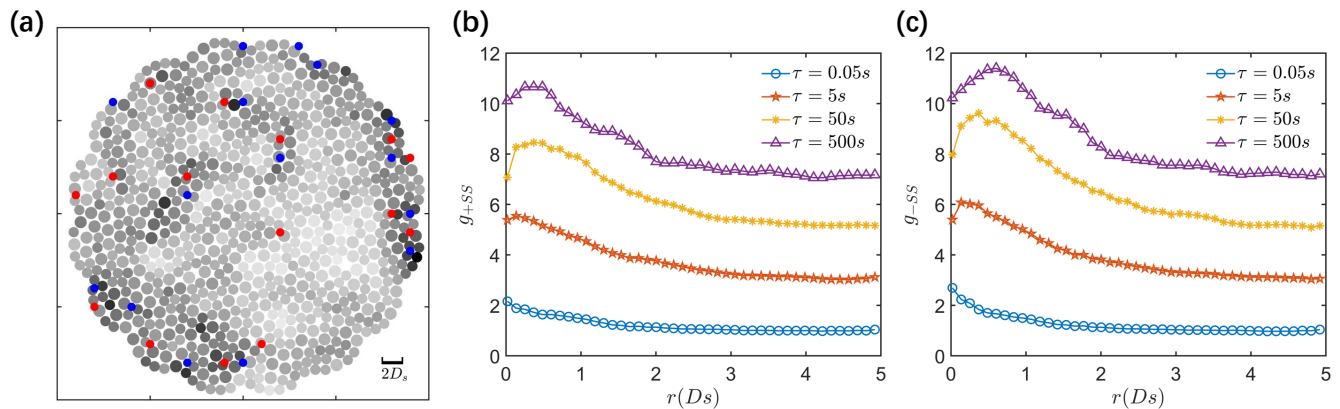


FIG. 3. **Structural relaxation towards the onset of collective motion is mediated by topological defects.** (a) Snapshot of D_{\min}^2 field (gray color map) with topological defects (red and blue symbols) at the observation time of $\tau = 500$ s. The characterization of local collective motion for the same τ is provided by the third panel in Fig. 2(a). (b) Pair correlation functions between areas of strong structural relaxation, soft spots (SS) (top 5% D_{\min}^2 particles), and positive topological defects at time interval τ . (c) The same correlation functions for negative topological defects. Each curve has been shifted up by two units on the vertical axis for clearer visualization.

whose thicknesses represent their amplitudes. These different timescales are taken as benchmark values to characterize our system's short-, intermediate-, and long-term dynamics.

Looking at the spatial structure of the displacements, it is clear that at short time scales ($\tau = 0.05$ s in Fig. 2), the motion of the particles is uncorrelated, random and independent, as in a gas-like environment. Kinematically, this is the consequence of the activity injecting kinetic energy at the individual particle level and favoring a two-dimensional (2D) Brownian motion similar to the effect of temperature in thermal systems. Observing the dynamics on longer time scales makes the emergence of collective motion and large-scale cooperative structures evident. As we argue below, this emergence can be ascribed to the inelastic interparticle collisions and rationalized by topological concepts applied to the displacement vector field.

In Fig. 2(a), we show the value of the local displacement polarization P_c using a color map ranging from blue ($P_c = 0$) to yellow ($P_c = 1$). Thus, yellow regions represent clusters with strong collective motion, where the particle displacements are aligned as flocks of birds. As the observation time increases, from the left to right panels, the size of the cooperative (yellow) regions grows, indicating the emergence of larger-scale collective motion. To provide a microscopic explanation of this behavior, we present the location of the topological defects (TDs) in the same panels, using red symbols for vortices and blue symbols for anti-vortices. We notice that at short times ($\tau = 0.05$ s), the topological defects are located in random positions, forming a gas of defects. Moreover, TDs tend to be located in regions with low polarization, indicating that TDs are microscopic objects that disrupt the onset of collective motion by randomizing the direction of the particle displacements. More details on the spatial

correlation between TDs as a function of the observation time τ can be found in Appendix B.

Importantly, we observe that the onset of collective motion, characterized by the percolation of clusters with large P_c , is mediated by the annihilation of topological defects that 'live' at the interfaces between these collective clusters (blue regions). This annihilation occurs between pairs of defects with opposite charges, preserving the total winding number q_{tot} . Two examples of this process are shown with enlarged views in Fig. 2(b). It is also evident and discussed in more detail below that the number of TDs decreases with the observation time, favoring the establishment of large-scale collective clusters.

To provide a complementary view of these dynamics, in Fig. 2(c), we present the same particle displacements and TDs but, this time, superimposed onto the amplitude of the local displacement curl Ω_l . As expected, the local curl color map (Fig. 2(b)) and the local polarization color map (Fig. 2(a)) are roughly complementary. Moreover, the local curl Ω_l is significant around the TDs, that can therefore be identified as the microscopic objects disrupting the irrotational nature of the displacement field. In this complementary view, the onset of collective motion is driven by the percolation of areas with low local displacement curl, which again is driven by the annihilation of defect pairs (Fig. 2(c)).

RELAXATION TOWARDS A NON-EQUILIBRIUM STEADY STATE IS MEDIATED BY TOPOLOGICAL DEFECTS

As discussed in the previous Section and shown in Fig. 2, topological defects appear at the interface between regions with highly collective motion, and their annihilation is the microscopic mechanism behind the onset of

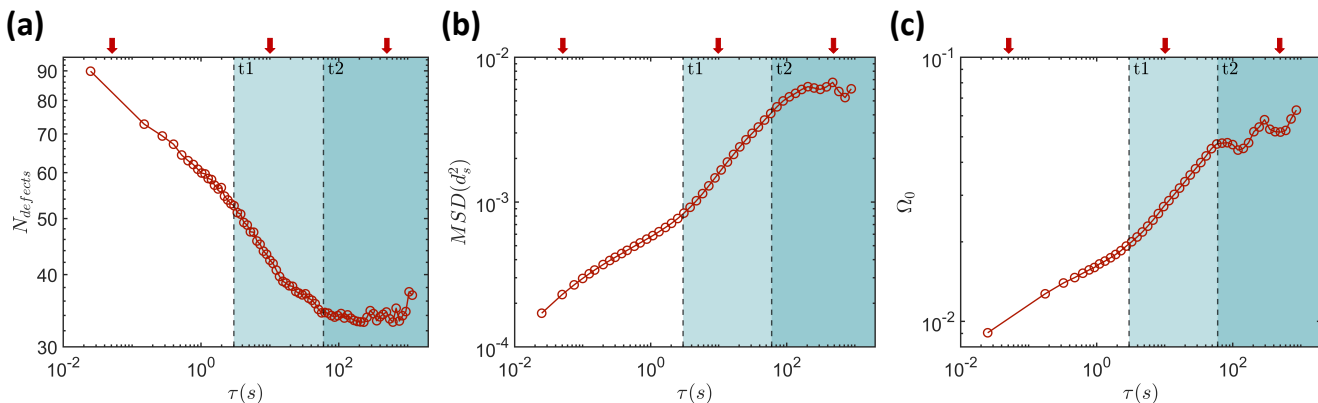


FIG. 4. **Three stage non-equilibrium dynamics.** (a): **Topological signatures.** Defect statistics as a function of the observation time τ . N_{defects} is the total number of TDs. The vertical dashed lines indicate the two time scales $t_1 = 3$ s, $t_2 = 60$ s. (b): **Particle-level dynamics.** Mean square displacement (MSD) in units of the square of the small particle diameter d_s^2 . (c): **Collective motion.** Average curl of the system Ω_0 . The three red arrows at each panel correspond to the selected times shown in Fig. 2.

large-scale structures in the dynamics. As a result, the relaxation towards the final non-equilibrium steady state is concentrated at the interface between these regions (*e.g.*, yellow areas in Fig. 2(a)).

To explore this physical mechanism further, we calculate D_{min}^2 , which quantifies the strength of nonaffine particle displacements between two consecutive configurations (see Methods A for details) [74]. A large value for this quantity represents soft areas in the sense that structural relaxation is more intense than elsewhere. In Fig. 3(a), we calculate the intensity of D_{min}^2 projected on each particle for $\tau = 500$ s using a gray color map, with darker regions representing larger values of D_{min}^2 . By visually comparing this color map with that presented in the third panel of Fig. 2(a), it is clear that regions with large D_{min}^2 correspond to smaller values of P_c . This implies that areas with strong structural relaxation are those where motion is still random and poorly collective.

In Fig. 3(a), we represent the topological defects (TDs) with charges $+1$ and -1 using blue and red symbols, respectively. These TDs appear in pairs within regions of higher D_{min}^2 values. To quantify this observation, we define ‘soft spots’ (SS) as the top 5% of particles with the highest D_{min}^2 values and analyze their positional correlation with both positive and negative defects. The results are shown in Fig. 3(b) and (c). Each curve exhibits a peak at small r , with the peak height increasing slightly over time. This suggests a strong short-range correlation between soft spots and TDs. The correlation is slightly stronger for negative defects, though the difference is not substantial. This could be explained by the fact that TDs typically appear in pairs, which may balance out the correlation differences. Overall, the observations in Fig. 3 suggest that topological defects play a key role in the system’s structural relaxation and mediate the emergence of collective motion during out-of-equilibrium dynamics.

We also notice that the strong correlation between structural relaxation (D_{min}^2) and topological vortex-like defects is reminiscent of recent results in 2D amorphous solids and defective crystals in which these objects have been proposed as the microscopic carriers of plasticity [75–80].

THREE STAGE NON-EQUILIBRIUM DYNAMICS

We investigate the non-equilibrium dynamics of the system across a full range of observation times, spanning six decades from $\tau = 10^{-2}$ s to $\tau = 10^4$ s, and reveal a three-stage evolution that is evident in both topological characteristics, particle level dynamics, and collective motion. Three snapshots of the system dynamics in each of these stages have already been presented in Fig. 2 (see vertical red arrows in Fig. 4).

In Fig. 4(a), we track the evolution of topological defects at different time scales. Up to a characteristic time scale of $t_1 \approx 3$ s, the total number of defects, N_{defects} , decreases monotonically over time, indicating frequent and intermittent annihilation events. Beyond t_1 , coinciding with the strengthening of collective motion shown in Fig. 2, the dynamics of TDs accelerate as the average collective cluster size increases. Consequently, the total number of defects declines at a faster rate. At a second characteristic time scale, $t_2 \approx 60$ s, the system reaches a non-equilibrium steady state, likely due to a balance between activity and inelastic interactions. Beyond this point, the number of topological defects remains relatively constant. Simultaneously, large vortex clusters begin to percolate through the space, culminating in a dominant vortex-like structure particularly visible at the center of the third panel in Fig. 2(a).

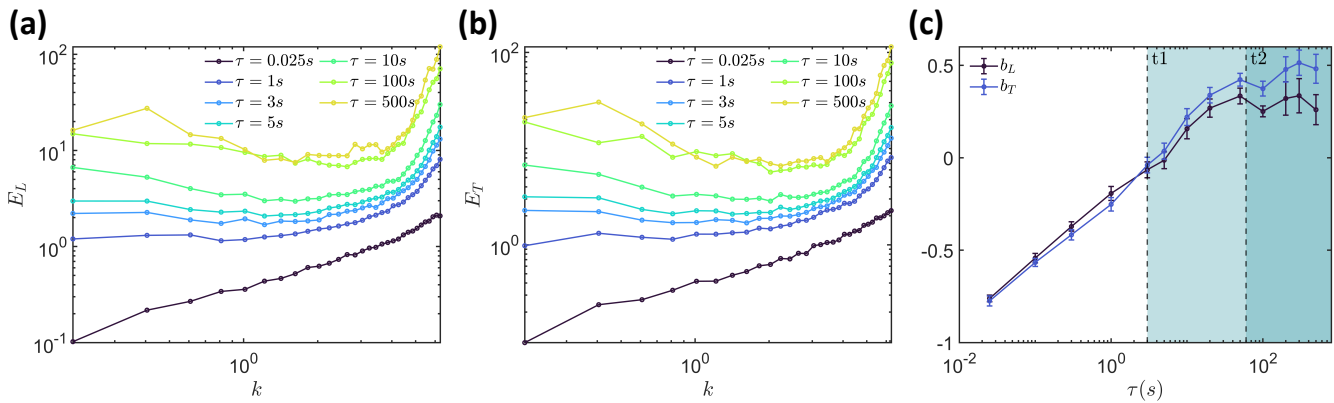


FIG. 5. **Turbulent-like energy cascades as revealed by energy power spectra.** Longitudinal (a) and transverse (b) kinetic energy spectra at different observation times τ as a function of the wave number k . (c) Power-law exponents b for longitudinal (b_L) and transverse spectra (b_T).

Figure 4(b) displays the mean square displacement (MSD), where the unit length is given in terms of the small particle diameter (d_s). This quantity characterizes the system's dynamics at the particle level. The MSD evolution follows three distinct stages. For $t < t_1$, the MSD exhibits sub-diffusive behavior, $\text{MSD} \propto t^{0.32}$, indicating that particle motion is constrained within a ‘cage’ on short timescales. Between t_1 and t_2 , as the total number of TDs, N_{defects} , decreases more rapidly, particle dynamics accelerate while maintaining sub-diffusive characteristics with a different exponent, $\text{MSD} \sim t^{0.55}$. This regime coincides with the increasing mean cluster size of collective motion, as observed in the second snapshot of Fig. 2(a). Beyond t_2 , particle dynamics slow as the system reaches a non-equilibrium steady state, where the MSD approaches a plateau. This trend aligns with the stabilization of the total number of defects, confirming that defects mediate local relaxation. Ultimately, the system attains a collective steady state, emerging from the interplay between activity (energy injected through vibrations) and inelastic collisions.

To further investigate the relationship between the formation of vortices in the system and its collective dynamics, we calculate the average curl Ω_0 of the displacement field, defined as

$$\Omega_0 = \sqrt{\left\langle \frac{1}{N} \sum_l (\nabla \times \mathbf{u}_l)^2 \right\rangle}. \quad (4)$$

As shown in Fig. 4(c), this quantity also shows a characteristic three-stage evolution. It slowly increases before t_1 , rises rapidly between t_1 and t_2 , and reaches a steady state after t_2 . The average curl behavior is consistent with the defect numbers and MSD, confirming the previous physical picture.

In conclusion, the number of defects, MSD, and average curl exhibit three distinct dynamical stages, establishing a link between topology, particle-level dynamics, and collective motion. These quantities are inter-

related: at short time scales ($t < t_1$), particle motion is ‘trapped’ due to frequent collisions, resulting in slow sub-diffusion in the MSD. Rapid fluctuations in the displacement field, driven by collisions, lead to efficient defect annihilation, causing a continuous decrease in defect numbers. Between t_1 and t_2 , the system's dynamics evolve more rapidly, driven by the formation of larger vortices in the displacement field. During this period, the defect number decreases at an accelerated rate. After t_2 , the system reaches a steady state, where the number of defects, MSD, and average curl stabilize over time. The average curl attains its maximum value, signifying the emergence of stable large vortices. This accounts for the total topological number approaching a plateau and the onset of large-scale collective motion. Defects regulate local structural rearrangements, ultimately culminating in the emergence of large vortices over long timescales.

TURBULENT-LIKE ENERGY CASCADES

The non-equilibrium characteristics of vortices offer a microscopic perspective on the system's dynamics and the emergence of large-scale collective motion in the final non-equilibrium steady state. Kinematically, the transition to this steady state is governed by the interplay between activity and inelastic collisions. As energy is injected at short scales (*i.e.*, the particle level), the emergence of self-organized collective motion necessitates an energy transfer from small to large scales, a hallmark of turbulent-like inverse cascades. In fluid mechanics, the inverse energy cascade was first introduced to describe the spatial-temporal chaotic flow dynamics in 2D turbulence, considering the conservation of kinetic energy and mean squared vorticity in the inertial range where energy dissipation is negligible. This phenomenon was first predicted in the late 1960's by Kraichnan [81] and later confirmed by numerous studies (*e.g.*, [82–86]). A notable natural example of this process is the formation

of massive quasi-2D structures, such as hurricanes.

To test this hypothesis, we define the kinetic energy spectra,

$$E_L(k) \equiv 2\pi k \left\langle \frac{1}{N} \left| \sum_{j=1}^N u_{j,\parallel} e^{-i\mathbf{k}\cdot\mathbf{r}_j} \right|^2 \right\rangle, \quad (5)$$

$$E_T(k) \equiv 2\pi k \left\langle \frac{1}{N} \left| \sum_{j=1}^N u_{j,\perp} e^{-i\mathbf{k}\cdot\mathbf{r}_j} \right|^2 \right\rangle, \quad (6)$$

where N is the number of particles in the system. $u_{j,\parallel}$ and $u_{j,\perp}$ are the components of the displacement vector of a particle j parallel and perpendicular concerning the wave vector \mathbf{k} and i is the imaginary unit. L and T stand respectively for “longitudinal” and “transverse”.

Our experimental results are presented in Fig. 5(a, b) at various time scales, denoted as τ . At large wave vectors—or equivalently, very short length scales—the curves are strongly affected by the static structure factor, which arises from the hard-disk interactions in our granular system. This factor typically exhibits a peak around $k \approx 2\pi$, though it is not displayed in the figure. It is important to note that the unit of length is expressed in terms of the small particle diameter d_s . Moreover, as the observation time τ increases, the influence of the static structure factor becomes more pronounced. This occurs because the spectra $E_L(k)$ and $E_T(k)$ are computed using the displacement field rather than the velocity field. Consequently, this would introduce a τ dependent scaling prefactor for $E_L(k)$ and $E_T(k)$, revealing that kinetic energy fluctuations diminish as a function of τ . As a result, at larger observation times, the effect of the static structure factor becomes increasingly evident around particle scales.

Nevertheless, a clear trend emerges in the intermediate and low range of k . In particular, at short times, both E_L and E_T grow with k , flattening in an intermediate τ range and then changing their slope at late times. To better characterize this behavior, we fit the various curves with a power-law ansatz $E_{L,T} \propto k^{-b_{L,T}}$. The extracted power-law exponent is presented in Fig. 5(c) as a function of the observation time τ . Below t_1 , we observe that $b_{L,T}$ are approximately identical and both negative, signaling a spectrum that grows towards smaller scales. Around t_1 , the spectrum starts to flatten, and the power-law exponents become slightly positive, presenting differences between the longitudinal and transverse sectors. Finally, above t_2 , the power-law exponents reach a plateau value in approximately $b_L \approx 0.3$ and $b_T \approx 0.4$.

This kinematic behavior aligns well with the three-stage dynamics presented in Fig. 4 and can be rationalized as follows. At short time scales, the energy injected by the active driving is gradually transferred to the individual particles, inducing a direct energy cascade towards microscopic scales. Around $t_1 \approx 3s$, energy is evenly distributed across all scales, corresponding to the highest

degree of dynamical heterogeneities. When the observation time exceeds $3s$, energy starts transferring from small to larger scales, exhibiting a turbulent-like inverse cascade. This process becomes steady around $t_2 \approx 60s$ when the energy transfer becomes roughly independent of time.

The results in Fig. 5 reveal intriguing scaling behaviors, prompting further investigation into the underlying physical mechanisms. A natural question arises: what physical mechanism is responsible for this behavior? In 2D turbulence, the theory of inverse energy cascade assumes the conservation of mean kinetic energy and mean squared vorticity in the inertial range [81]. In our active granular system, not all kinetic energy is transferred from small to large scales due to strong dissipation caused by inelastic collisions and friction. Nevertheless, as we will argue below, a similar principle governs the self-organization dynamics in our system, leading to a turbulent-like inverse energy cascade.

In Fig. 4(c), the mean curl of the displacement field, Ω_0 , exhibits two distinct power-law scaling behaviors in the first two regimes when $\tau < t_2$, following $\Omega_0 \propto \tau^\alpha$ with $\alpha = 0.15$ for $\tau < t_1$ and $\alpha = 0.3$ for $t_1 < \tau < t_2$. The quantity Ω_0 , which characterizes the displacement field \mathbf{u} over an observation time τ , differs from vorticity in 2D turbulence in two key aspects. First, in turbulence, vorticity is derived from the velocity field, $\Omega \equiv \nabla \times \mathbf{v}$, rather than the displacement field. In a fluid system, the two quantities are directly proportional only at sufficiently short observation times. However, in a granular system, the cascade process is further complicated by inelastic collisions and friction, which prevent full energy transfer across scales. Second, the displacement field \mathbf{u} exhibits a nontrivial dependence on τ .

We assume that the mean squared vorticity, $\overline{\Omega^2}$, follows $\overline{\Omega^2} \propto (\Omega_0/\tau^\alpha)^2$. By definition, this implies $\overline{\Omega^2} \propto \tau^{-2\alpha} \mathbf{u}_l^2$ from dimensional analysis. Estimating \mathbf{u}_l^2 from the MSD results in Fig. 4(b), we obtain $\mathbf{u}_l^2 \propto \tau^\beta$, with $\beta = 0.3$ for $\tau < t_1$ and $\beta = 0.55$ for $t_1 < \tau < t_2$. This leads to $\overline{\Omega^2} \propto \tau^{\beta-2\alpha}$. Notably, the exponent $\beta - 2\alpha \approx 0$ for both $\tau < t_1$ and $t_1 < \tau < t_2$. These findings suggest that the mean squared vorticity is nearly conserved in the turbulent-like inverse energy cascade of our active granular system, adhering to a principle akin to that of 2D turbulence.

PACKING-FRACTION CONTROLLED INTERPLAY BETWEEN ACTIVITY AND INTERACTIONS

We conducted experiments at various packing fractions to gain deeper insights into the collective behavior of the system and the competition between activity and inelastic collisions (see Fig. 1).

Our initial analysis focused on the highest packing fraction ($\phi = 0.822$), where strong inelastic collisions balance the effects of activity, resulting in a late-time non-

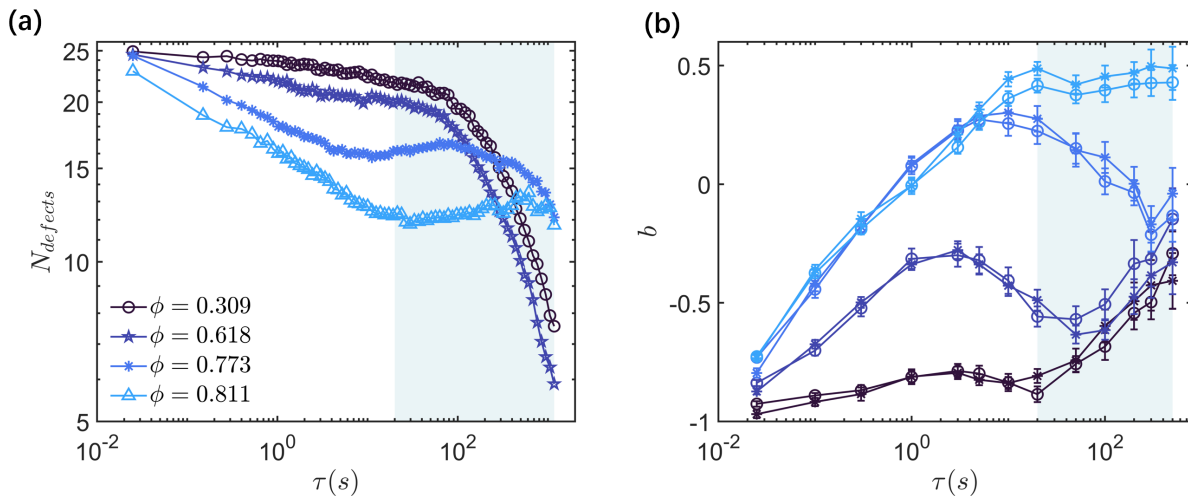


FIG. 6. **Activity versus interactions and non-equilibrium steady state formation.** (a): Defect statistics as a function of the observation time τ for different packing fractions ϕ . All previous figures refer to the highest packing fraction $\phi = 0.822$. N_{defects} is the total number of TDs. (b): Power-law exponents b for energy spectra. The color scheme refers to the different packing fractions shown in panel (a). Open circles denote the longitudinal component b_L and stars the transverse component b_T . The background color in both panels indicate the onset of the non-equilibrium steady state at high packing fraction, to be contrasted with its absence at low ϕ .

equilibrium steady state. Here, we extend the analysis to the lowest packing fraction ($\phi = 0.309$), where the dynamics remain decorrelated and gas-like due to the weak inelastic interactions [38].

Figure 6(a) shows the evolution of the total number of topological defects, N_{defects} , for four packing fractions ($\phi = 0.309, 0.618, 0.773$, and 0.811). At a high packing fraction ($\phi = 0.811$), the behavior of N_{defects} resembles that observed at the maximal packing fraction shown in Fig. 4(a).

The instability of the non-equilibrium steady state becomes evident at $\phi = 0.773$, where the system only forms a transient plateau before decaying at late times. Notably, this late-time decay is significantly faster than the initial short-time decay, a pattern also observed at the two lower packing fractions.

At the lower packing fractions ($\phi = 0.309$ and $\phi = 0.618$), the number of defects decreases monotonically, exhibiting a two-step relaxation mechanism without ever reaching a non-equilibrium steady state. This can be attributed to the diminishing intensity of inelastic interactions as the packing fraction decreases. Since these interactions are crucial for establishing collective motion by balancing the random effects of activity (see Fig. 1), their weakness in these dilute systems prevents the formation of a steady state, as reflected by the continuous decline in the number of defects.

To validate this interpretation, Fig. 6(b) presents the power-law exponents for turbulent-like energy cascades in active granular fluids across the four packing fractions. At the lower packing fractions ($\phi = 0.309$ and $\phi = 0.618$), the power-law exponents b remain negative throughout the observation period, indicating that energy transfer

from small to large scales never occurs. The absence of this inverse cascade underscores the system's inability to form a stable steady state characterized by constant values for both the longitudinal and transverse components of b . This finding emphasizes that the inverse energy cascade, driven by topological defect dynamics, is fundamental to establishing a non-equilibrium steady state with emergent large-scale collective motion.

For the intermediate packing fraction ($\phi = 0.773$), the power-law exponents reach positive values but fail to stabilize over long timescales, indicating an increased yet insufficient attempt to achieve collective behavior. In contrast, at the high packing fraction ($\phi = 0.811$), the power-law exponents continue to rise and eventually plateau over extended timescales, as shown within the blue-shaded region of Fig. 6(b).

This comprehensive analysis highlights the interplay between activity and interactions. At low packing fractions, weak inelastic collisions allow activity to dominate, injecting energy at microscopic scales without propagating to larger ones. As a result, the system remains decorrelated and fails to form a non-equilibrium steady state. In contrast, at high packing fractions, interactions gradually balance with activity, enabling energy transfer to larger scales and the formation of collective motion. Remarkably, fully established collective motion is observed only for $\phi = 0.811$ and $\phi = 0.822$, aligning with previous studies that identified liquid-like collective behavior at these packing fractions [38]. This balance between activity and inelastic interactions likely gives rise to liquid-like collective dynamics, suggesting that the late-time steady state behaves similarly to a thermal liquid [87, 88].

CONCLUSIONS

Using active granular disks as a model for nonpolar dry active Brownian particles, we conducted a comprehensive experimental study to investigate the topological features that give rise to steady-state large-scale collective dynamics and turbulent-like inverse energy cascades. The dynamical behavior of the system evolves through a packing fraction-controlled interplay between activity and particle interactions.

Activity at the particle level converts the injected mechanical energy into Brownian-like stochastic motions, while particle-particle interactions, driven by inelastic collisions and friction, promote coherent motion. At sufficiently high packing fractions, the effects of inelastic collisions gradually dominate over active contributions as observation time increases, leading to the emergence of large-scale collective motion.

This self-organization occurs through structural rearrangements mediated by topological defects, including the annihilation of positive and negative defects and the formation of large vortices. The number of defects, the mean squared displacement of the system, and the average curl of the displacement field together reveal coherent three-stage dynamics, highlighting the essential role of defects in the system's evolution. From a kinematic perspective, defect annihilation and the creation of large-scale collective regions are associated with a turbulent-like inverse energy cascade, where energy transfers from small to large scales.

Our study demonstrates how large-scale collective motion emerges from a homogeneous ensemble of nonpolar Brownian particles, offering new insights into collective dynamics in biological and robotic systems, such as insect swarms, bird flocks, and robotic swarms.

ACKNOWLEDGMENTS

CJ and MB acknowledge the support of the Shanghai Municipal Science and Technology Major Project (Grant No.2019SHZDZX01). MB acknowledges the support of the sponsorship from the Yangyang Development Fund. ZZ, YC and JZ acknowledge the support of the NSFC (No. 11974238 and No. 12274291) and the Shanghai Municipal Education Commission Innovation Program under No. 2021-01-07-00-02-E00138. ZZ, YC and JZ also acknowledge the support from the Shanghai Jiao Tong University Student Innovation Center.

Appendix A: Methods

1. Identification of topological defects

The topological defects are defined using the discrete displacement field. The vortex detection algorithm steps

around the 2×2 square in the conventional counter-clockwise sense, computing the phase gradient, *i.e.*, the difference values in displacement. When the modulus of this difference $|\Delta\chi|$ exceeds π , the phase is unwrapped. Then p , the detected winding number is found such that the phase gradient is $2p\pi - \Delta\chi \mapsto \Delta\xi$, where $p \in \mathbb{Z}$ and $\Delta\xi \in (-\pi, \pi]$ [89]. The value of p corresponds to the detected charge numbers: +1, 0, and -1. +1 corresponds to a positive topological defect, while -1 corresponds to a negative topological defect.

2. Characterization of structural rearrangements

The characterization of structural arrangements is performed using the well-established concept of D_{\min}^2 [74], that allows for a direct identification of regions with large non-affine displacement.

In order to do that, we define

$$D^2(t, \Delta t) = \sum_n \sum_i \left(r_n^i(t) - r_0^i(t) - \sum_j (\delta_{ij} + \varepsilon_{ij}) \times [r_n^j(t - \Delta t) - r_0^j(t - \Delta t)] \right)^2, \quad (\text{A1})$$

where the indices i and j represents spatial coordinates, while n indexes the particles within the interaction range of the reference particle, with $n = 0$ being the reference particle. $r_n^i(t)$ denotes the i th component of the position of the n th particle at time t . The ε_{ij} that minimizes D^2 is then determined by calculating

$$X_{ij} = \sum_n [r_n^i(t) - r_0^i(t)] \times [r_n^j(t - \Delta t) - r_0^j(t - \Delta t)], \quad (\text{A2})$$

$$Y_{ij} = \sum_n [r_n^i(t - \Delta t) - r_0^i(t - \Delta t)] \times [r_n^j(t - \Delta t) - r_0^j(t - \Delta t)], \quad (\text{A3})$$

$$\varepsilon_{ij} = \sum_k X_{ik} Y_{jk}^{-1} - \delta_{ij}. \quad (\text{A4})$$

The minimum value of $D(t, \Delta t)$ defines D_{\min}^2 that quantifies the local deviation from affine deformation during a time interval $[t - \Delta t, t]$. D_{\min}^2 is an excellent diagnostic for identifying local irreversible deformations and structural rearrangements.

Appendix B: Spatial structure of topological defects

We characterize the spatial structure of the topological defects by investigating their radial pair correlation functions $g_{\alpha\beta}(r)$, where $\alpha, \beta = \pm$ indicate the sign of the corresponding winding number.

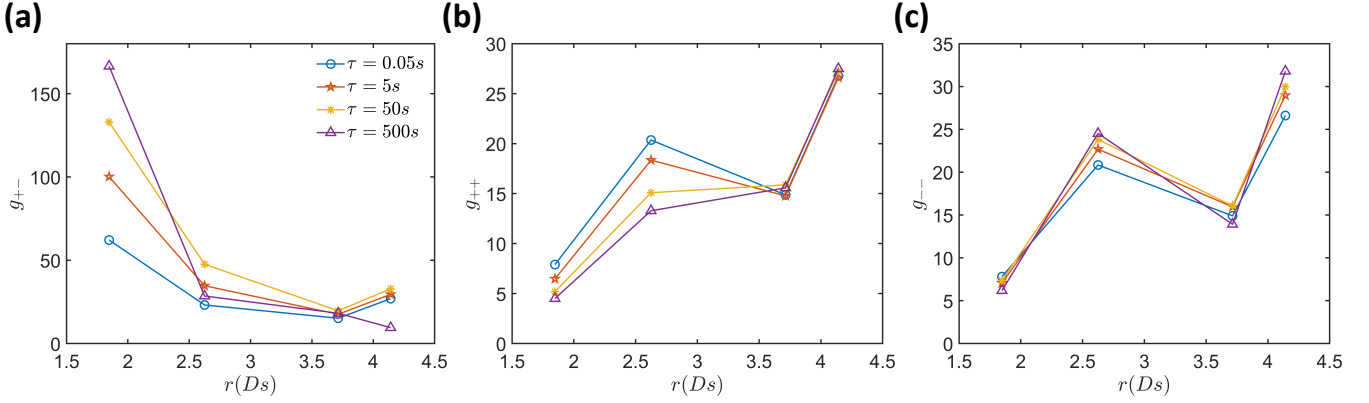


FIG. 7. **Spatial correlation of topological defects.** Pair correlation function of positive and negative defects (a), positive and positive defects (b), negative and negative defects (c) for different values of the observation time τ .

The radial pair correlation function between topological defects with α and β charges is defined as

$$g_{\alpha\beta}(r) = \frac{L_x L_y}{2\pi r N_\alpha N_\beta} \sum_{i=1}^{N_\alpha} \sum_{j=1}^{N_\beta} \delta(r - |\vec{r}_{ij}|), \quad (\text{B1})$$

where L_x, L_y are the dimensions of the region in which correlation is calculated, $N_{\alpha\beta}$ is the number of defects with α, β charge inside the region, and $|\vec{r}_{ij}|$ is the distance between topological defects.

We display our results in Fig. 7. First, we observe that at any observation time, TDs with opposite charge shows a strong short-range correlation, with a large value of g_{\pm} at the first lattice point. This indicates that opposite-sign defects tend to stay close to and attract each other, forming pairs with zero total winding number. On the other hand, the correlations between TDs with same charge do not show a peak at short length-scales. In contrast, as shown in Fig. 7(b) and (c), for defects of the same sign, the value at the first lattice point is low, suggesting that same-sign defects tend to repel each other.

Moreover, as shown in Fig. 7(a), the short range correlation between + and - TDs becomes more pronounced at late time, with the first peak in g_{\pm} being much larger for long τ . This suggests that, while the system relaxes towards the final non-equilibrium steady state, the TDs self-organize in short-range pairs and display a more ordered spatial distribution.

Appendix C: Relaxation dynamics and dynamical heterogeneities

In order to further study the dynamics of our system, we consider two typical probes: the intermediate scattering

function $F_s(q, t)$ and the four-point susceptibility $\chi_4(t)$.

The intermediate scattering function is defined as

$$F_s(q, t) = \frac{1}{N} \sum_{j=1}^N \left\langle e^{-i\vec{q} \cdot (\vec{r}_j(t) - \vec{r}_j(0))} \right\rangle, \quad (\text{C1})$$

where q is the wave vector, N is the total number of particles in the system, $r_j(t)$ is the position of particle j at time t . Results in Fig.8(a) show that system exhibits progressively slower relaxation by increasing packing fraction.

The four-point susceptibility in Fig.8(b) describes the degree of dynamical heterogeneity in space within a time interval, and is defined as: $\chi_4(t) = N[\langle q_s(t)^2 \rangle - \langle q_s(t) \rangle^2]$, where $q_s(t) = (1/N) \sum_{i=1}^N w(|r_i(t) - r_i(0)|)$, $w = 1(0)$ if $|r_i(t) - r_i(0)| < (>) 0.5D$. N is the total number of particles in the system, $r_i(t)$ is the position of particle i at time t , and D is the average particle diameter. The average $\langle \cdot \rangle$ is performed over all particles and all initial times. The peak position in $\chi_4(t)$ indicates the time during which the dynamics exhibit the greatest heterogeneity, while the peak height reflects the intensity of these heterogeneities. As the packing fraction increases, the time at which the system reaches its maximum dynamical heterogeneity is delayed. Meanwhile, from a packing fraction of $\phi = 0.309$ to 0.811 , the peak intensity of dynamical heterogeneity also increases. Due to experimental limitations, the data for $\phi = 0.822$ do not exhibit a distinct peak within the accessible observation time. However, we speculate that a peak would emerge over a longer time scale.

[1] M. Vrugt and R. Wittkowski, A review of active matter reviews, [arXiv e-prints](#), [arXiv:2405.15751](#) (2024).

[2] C. W. Reynolds, Flocks, herds and schools: A distributed

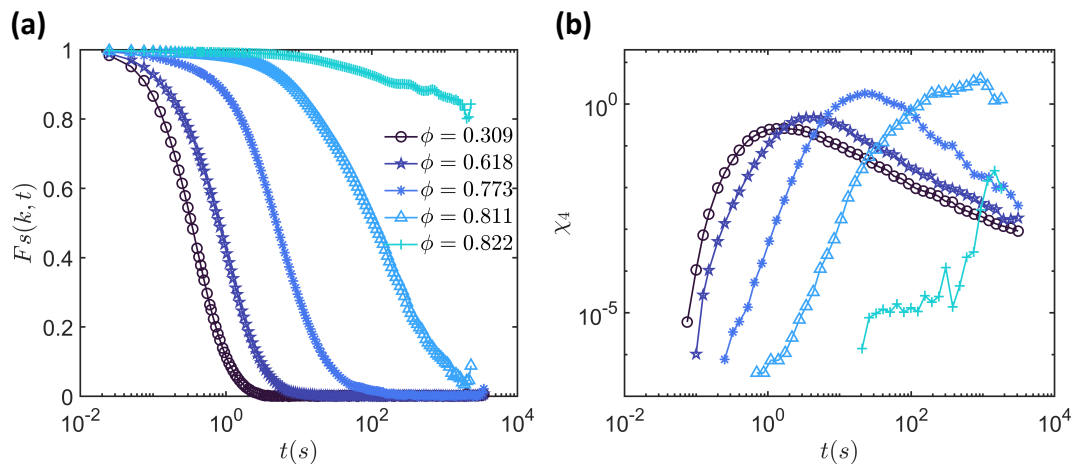


FIG. 8. **Dynamical characterization.** Intermediate scattering function $F_s(q, t)$ as a function of time for different packing fractions ϕ (a). Four point susceptibility function $\chi_4(t)$ as a function of time for the same values of the packing fraction ϕ (b). Same color scheme is adopted in both panels of this figure.

- behavioral model, in *Proceedings of the 14th Annual Conference on Computer Graphics and Interactive Techniques*, SIGGRAPH '87 (Association for Computing Machinery, New York, NY, USA, 1987) p. 25–34.
- [3] F. Gu, B. Guiselin, N. Bain, I. Zuriguel, and D. Bartolo, Emergence of collective oscillations in massive human crowds, *Nature* **638**, 112 (2025).
- [4] S. Ramaswamy, The mechanics and statistics of active matter, *Annu. Rev. Condens. Matter Phys.* **1**, 323 (2010).
- [5] M. J. Bowick, N. Fakhri, M. C. Marchetti, and S. Ramaswamy, Symmetry, thermodynamics, and topology in active matter, *Phys. Rev. X* **12**, 010501 (2022).
- [6] P. G. de Gennes, Granular matter: a tentative view, *Rev. Mod. Phys.* **71**, S374 (1999).
- [7] H. M. Jaeger, S. R. Nagel, and R. P. Behringer, Granular solids, liquids, and gases, *Rev. Mod. Phys.* **68**, 1259 (1996).
- [8] B. Andreotti, Y. Forterre, and O. Pouliquen, *Granular media: between fluid and solid* (Cambridge University Press, 2013).
- [9] T. Aste, M. Saadatfar, and T. J. Senden, Geometrical structure of disordered sphere packings, *Phys. Rev. E* **71**, 061302 (2005).
- [10] S. Torquato, T. M. Truskett, and P. G. Debenedetti, Is random close packing of spheres well defined?, *Phys. Rev. Lett.* **84**, 2064 (2000).
- [11] S. F. Edwards and R. B. S. Oakeshott, Theory of powders, *Physica A* **157**, 1080 (1989).
- [12] S. Henkes, C. S. O'Hern, and B. Chakraborty, Entropy and temperature of a static granular assembly: An ab initio approach, *Phys. Rev. Lett.* **99**, 038002 (2007).
- [13] A. Baule, F. Morone, H. J. Herrmann, and H. A. Makse, Edwards statistical mechanics for jammed granular matter, *Rev. Mod. Phys.* **90**, 015006 (2018).
- [14] C. S. O'Hern, L. E. Silbert, A. J. Liu, and S. R. Nagel, Jamming at zero temperature and zero applied stress: The epitome of disorder, *Phys. Rev. E* **68**, 011306 (2003).
- [15] A. J. Liu and S. R. Nagel, The jamming transition and the marginally jammed solid, *Annu. Rev. Condens. Matter Phys.* **1**, 347 (2010).
- [16] M. van Hecke, Jamming of soft particles: geometry, mechanics, scaling and isostaticity, *J. Phys.: Condens. Matter* **22**, 033101 (2010).
- [17] P. Charbonneau, J. Kurchan, G. Parisi, P. Urbani, and F. Zamponi, Fractal free energy landscapes in structural glasses, *Nat. Commun.* **5**, 3725 (2014).
- [18] P. Charbonneau, J. Kurchan, G. Parisi, P. Urbani, and F. Zamponi, Glass and jamming transitions: From exact results to finite-dimensional descriptions, *Annu. Rev. Condens. Matter Phys.* **8**, 265 (2017).
- [19] Y. Wang, J. Shang, Y. Jin, and J. Zhang, Experimental observations of marginal criticality in granular materials, *PNAS* **119**, e2204879119 (2022).
- [20] M. Wyart, Marginal stability constrains force and pair distributions at random close packing, *Phys. Rev. Lett.* **109**, 125502 (2012).
- [21] M. Müller and M. Wyart, Marginal stability in structural, spin, and electron glasses, *Annu. Rev. Condens. Matter Phys.* **6**, 177 (2015).
- [22] D. Bi, J. Zhang, B. Chakraborty, and R. P. Behringer, Jamming by shear, *Nature* **480**, 355 (2011).
- [23] D. Pan, Y. Wang, H. Yoshino, J. Zhang, and Y. Jin, A review on shear jamming, *Phys. Rep.* **1038**, 1 (2023).
- [24] T. S. Majmudar and R. P. Behringer, Contact force measurements and stress-induced anisotropy in granular materials, *Nature* **435**, 1079 (2005).
- [25] Y. Wang, Y. Wang, and J. Zhang, Connecting shear localization with the long-range correlated polarized stress fields in granular materials, *Nat. Commun.* **11**, 4349 (2020).
- [26] J. N. Nampoothiri, Y. Wang, K. Ramola, J. Zhang, S. Bhattacharjee, and B. Chakraborty, Emergent elasticity in amorphous solids, *Phys. Rev. Lett.* **125**, 118002 (2020).
- [27] W. Li and R. Juanes, Dynamic imaging of force chains in 3d granular media, *PNAS* **121**, e2319160121 (2024).
- [28] G. D. R. MiDi, On dense granular flows, *EUR. PHYS. J. E* **14**, 341 (2004).
- [29] P. Jop, Y. Forterre, and O. Pouliquen, A constitutive law for dense granular flows, *Nature* **441**, 727 (2006).

- [30] K. Kamrin and G. Koval, Nonlocal constitutive relation for steady granular flow, *Phys. Rev. Lett.* **108**, 178301 (2012).
- [31] F. Rietz, C. Radin, H. L. Swinney, and M. Schröter, Nucleation in sheared granular matter, *Phys. Rev. Lett.* **120**, 055701 (2018).
- [32] B. Kou, Y. Cao, J. Li, C. Xia, Z. Li, H. Dong, A. Zhang, J. Zhang, W. Kob, and Y. Wang, Granular materials flow like complex fluids, *Nature* **551**, 360 (2017).
- [33] J. Shang, Y. Wang, D. Pan, Y. Jin, and J. Zhang, The yielding of granular matter is marginally stable and critical, *PNAS* **121**, e2402843121 (2024).
- [34] J. Deseigne, O. Dauchot, and H. Chaté, Collective motion of vibrated polar disks, *Phys. Rev. Lett.* **105**, 098001 (2010).
- [35] N. Kumar, H. Soni, S. Ramaswamy, and A. K. Sood, Flocking at a distance in active granular matter, *Nat. Commun.* **5**, 4688 (2014).
- [36] V. Narayan, S. Ramaswamy, and N. Menon, Long-lived giant number fluctuations in a swarming granular nematic, *Science* **317**, 105 (2007).
- [37] C. Jiang, Z. Zheng, Y. Chen, M. Baggioli, and J. Zhang, Dispersionless flat mode and vibrational anomaly in active brownian vibrators induced by stringlike dynamical defects, *Phys. Rev. Lett.* **133**, 188302 (2024).
- [38] C. Jiang, Z. Zheng, Y. Chen, M. Baggioli, and J. Zhang, Experimental observation of gapped shear waves and liquid-like to gas-like dynamical crossover in active granular matter, *Commun. Phys.* **8**, 82 (2025).
- [39] C. Scholz and T. Pöschel, Velocity distribution of a homogeneously driven two-dimensional granular gas, *Phys. Rev. Lett.* **118**, 198003 (2017).
- [40] Y. Chen and J. Zhang, High-energy velocity tails in uniformly heated granular materials, *Phys. Rev. E* **106**, L052903 (2022).
- [41] Y. Chen and J. Zhang, Anomalous flocking in nonpolar granular brownian vibrators, *Nat. Commun.* **15**, 6032 (2024).
- [42] C. A. Weber, C. Bock, and E. Frey, Defect-mediated phase transitions in active soft matter, *Phys. Rev. Lett.* **112**, 168301 (2014).
- [43] S. Shankar, A. Souslov, M. J. Bowick, M. C. Marchetti, and V. Vitelli, Topological active matter, *Nat. Rev. Phys.* **4**, 380 (2022).
- [44] L. Tubiana, G. P. Alexander, A. Barbensi, D. Buck, J. H. Cartwright, M. Chwastyk, M. Cieplak, I. Coluzza, S. Čopar, D. J. Craik, M. Di Stefano, R. Everaers, P. F. Faísca, F. Ferrari, A. Giacometti, D. Goundaroulis, E. Haglund, Y.-M. Hou, N. Ilieva, S. E. Jackson, A. Japaridze, N. Kaplan, A. R. Klotz, H. Li, C. N. Likos, E. Locatelli, T. López-León, T. Machon, C. Micheletti, D. Michieletto, A. Niemi, W. Niemyska, S. Niewiecz-erzal, F. Nitti, E. Orlandini, S. Pasquali, A. P. Perlin-ska, R. Podgornik, R. Potestio, N. M. Pugno, M. Ravnik, R. Ricca, C. M. Rohwer, A. Rosa, J. Smrek, A. Souslov, A. Stasiak, D. Steer, J. Sułkowska, P. Sułkowski, D. W. L. Sumners, C. Svaneborg, P. Szymczak, T. Tarenzi, R. Travasso, P. Virnau, D. Vlassopoulos, P. Zihlerl, and S. Žumer, Topology in soft and biological matter, *Phys. Rep.* **1075**, 1 (2024), Topology in soft and biological matter.
- [45] K. Copenhagen, R. Alert, N. S. Wingreen, and J. W. Shaevitz, Topological defects promote layer formation in *Myxococcus xanthus* colonies, *Nat. Phys.* **17**, 211 (2021).
- [46] Y. Maroudas-Sacks, L. Garion, L. Shani-Zerbib, A. Livshits, E. Braun, and K. Keren, Topological defects in the nematic order of actin fibres as organization centres of Hydra morphogenesis, *Nat. Phys.* **17**, 251 (2021).
- [47] O. J. Meacock, A. Doostmohammadi, K. R. Foster, J. M. Yeomans, and W. M. Durham, Bacteria solve the problem of crowding by moving slowly, *Nat. Phys.* **17**, 205 (2021).
- [48] L. A. Hoffmann, L. N. Carenza, J. Eckert, and L. Giomi, Theory of defect-mediated morphogenesis, *Sci. Adv.* **8**, eabk2712 (2022).
- [49] T. H. Tan, J. Liu, P. W. Miller, M. Tekant, J. Dunkel, and N. Fakhri, Topological turbulence in the membrane of a living cell, *Nat. Phys.* **16**, 657 (2020).
- [50] K. Kawaguchi, R. Kageyama, and M. Sano, Topological defects control collective dynamics in neural progenitor cell cultures, *Nature* **545**, 327 (2017).
- [51] A. Chardac, L. A. Hoffmann, Y. Poupart, L. Giomi, and D. Bartolo, Topology-driven ordering of flocking matter, *Phys. Rev. X* **11**, 031069 (2021).
- [52] X.-Q. Shi and Y.-Q. Ma, Topological structure dynamics revealing collective evolution in active nematics, *Nat. Commun.* **4**, 3013 (2013).
- [53] H. Li, H. Chaté, M. Sano, X.-Q. Shi, and H. P. Zhang, Robust edge flows in swarming bacterial colonies, *Phys. Rev. X* **14**, 041006 (2024).
- [54] L. Giomi, M. J. Bowick, P. Mishra, R. Sknepnek, and M. Cristina Marchetti, Defect dynamics in active nematics, *Philosophical Transactions of the Royal Society A: Mathematical, Physical and Engineering Sciences* **372**, 20130365 (2014).
- [55] Y. Ota, K. Takata, T. Ozawa, A. Amo, Z. Jia, B. Kante, M. Notomi, Y. Arakawa, and S. Iwamoto, Active topological photonics, *Nanophotonics* **9**, 547 (2020).
- [56] K. Sone, K. Yokomizo, K. Kawaguchi, and Y. Ashida, Hermitian and non-hermitian topology in active matter, *arXiv e-prints*, arXiv:2407.16143 (2024).
- [57] L. Giomi, Geometry and topology of turbulence in active nematics, *Phys. Rev. X* **5**, 031003 (2015).
- [58] T. Sanchez, D. T. N. Chen, S. J. DeCamp, M. Heymann, and Z. Dogic, Spontaneous motion in hierarchically assembled active matter, *Nature* **491**, 431 (2012).
- [59] L. Giomi, M. J. Bowick, X. Ma, and M. C. Marchetti, Defect annihilation and proliferation in active nematics, *Phys. Rev. Lett.* **110**, 228101 (2013).
- [60] L. M. Pismen, Dynamics of defects in an active nematic layer, *Phys. Rev. E* **88**, 050502 (2013).
- [61] S. Shankar, S. Ramaswamy, M. C. Marchetti, and M. J. Bowick, Defect unbinding in active nematics, *Phys. Rev. Lett.* **121**, 108002 (2018).
- [62] S. Shankar and M. C. Marchetti, Hydrodynamics of active defects: From order to chaos to defect ordering, *Phys. Rev. X* **9**, 041047 (2019).
- [63] F. C. Keber, E. Loiseau, T. Sanchez, S. J. DeCamp, L. Giomi, M. J. Bowick, M. C. Marchetti, Z. Dogic, and A. R. Bausch, Topology and dynamics of active nematic vesicles, *Science* **345**, 1135 (2014).
- [64] G. Duclos, C. Erlenkämper, J.-F. Joanny, and P. Silberzan, Topological defects in confined populations of spindle-shaped cells, *Nat. Phys.* **13**, 58 (2017).
- [65] S. Shankar, L. V. D. Scharrer, M. J. Bowick, and M. C. Marchetti, Design rules for controlling active topological defects, *PNAS* **121**, e2400933121 (2024), <https://www.pnas.org/doi/pdf/10.1073/pnas.2400933121>.

- [66] R. Zhang, A. Mozaffari, and J. J. de Pablo, Logic operations with active topological defects, *Sci. Adv.* **8**, eabg9060 (2022).
- [67] S. Li, B. Dutta, S. Cannon, J. J. Daymude, R. Avinery, E. Aydin, A. W. Richa, D. I. Goldman, and D. Randall, Programming active cohesive granular matter with mechanically induced phase changes, *Sci. Adv.* **7**, eabe8494 (2021).
- [68] T. B. Saw, A. Doostmohammadi, V. Nier, L. Kocgozlu, S. Thampi, Y. Toyama, P. Marcq, C. T. Lim, J. M. Yeomans, and B. Ladoux, Topological defects in epithelia govern cell death and extrusion, *Nature* **544**, 212 (2017).
- [69] P. Guillamat, J. Ignés-Mullol, and F. Sagués, Control of active liquid crystals with a magnetic field, *PNAS* **113**, 5498 (2016).
- [70] S. Fumeron and B. Berche, Introduction to topological defects: from liquid crystals to particle physics, *The European Physical Journal Special Topics* **232**, 1813 (2023).
- [71] T. Vicsek, A. Czirók, E. Ben-Jacob, I. Cohen, and O. Shochet, Novel type of phase transition in a system of self-driven particles, *Phys. Rev. Lett.* **75**, 1226 (1995).
- [72] L. Caprini and H. Löwen, Flocking without alignment interactions in attractive active brownian particles, *Phys. Rev. Lett.* **130**, 148202 (2023).
- [73] M. E. Cates and J. Tailleur, Motility-induced phase separation, *Annu. Rev. Condens. Matter Phys.* **6**, 219 (2015).
- [74] M. L. Falk and J. S. Langer, Dynamics of viscoplastic deformation in amorphous solids, *Phys. Rev. E* **57**, 7192 (1998).
- [75] Z. W. Wu, Y. Chen, W.-H. Wang, W. Kob, and L. Xu, Topology of vibrational modes predicts plastic events in glasses, *Nat. Commun.* **14**, 2955 (2023).
- [76] M. Baggioli, Topological defects reveal the plasticity of glasses, *Nat. Commun.* **14**, 2956 (2023).
- [77] P. Desmarchelier, S. Fajardo, and M. L. Falk, Topological characterization of rearrangements in amorphous solids, *Phys. Rev. E* **109**, L053002 (2024).
- [78] A. Bera, M. Baggioli, T. C. Petersen, T. W. Sirk, A. C. Liu, and A. Zaccone, Clustering of negative topological charges precedes plastic failure in 3d glasses, *PNAS Nexus* **3**, pgae315 (2024).
- [79] V. Vaibhav, A. Bera, A. C. Liu, M. Baggioli, P. Keim, and A. Zaccone, Experimental identification of topological defects in 2d colloidal glass, *Nat. Commun.* **16**, 55 (2025).
- [80] L.-Z. Huang, Y.-J. Wang, and M. Baggioli, Spotting structural defects in crystals from the topology of vibrational modes, *arXiv preprint arXiv:2410.04720* (2024).
- [81] R. H. Kraichnan, Inertial ranges in two-dimensional turbulence, *Phys. Fluids* **10**, 1417 (1967).
- [82] E. D. Siggia and H. Aref, Point-vortex simulation of the inverse energy cascade in two-dimensional turbulence, *Phys. Fluids* **24**, 171 (1981).
- [83] U. Frisch and P. Sulem, Numerical simulation of the inverse cascade in two-dimensional turbulence, *Phys. Fluids* **27**, 1921 (1984).
- [84] M. A. Rutgers, Forced 2d turbulence: Experimental evidence of simultaneous inverse energy and forward enstrophy cascades, *Phys. Rev. Lett.* **81**, 2244 (1998).
- [85] M. Rivera and X. L. Wu, External dissipation in driven two-dimensional turbulence, *Phys. Rev. Lett.* **85**, 976 (2000).
- [86] J. Paret and P. Tabeling, Experimental observation of the two-dimensional inverse energy cascade, *Phys. Rev. Lett.* **79**, 4162 (1997).
- [87] K. Trachenko and V. V. Brazhkin, Collective modes and thermodynamics of the liquid state, *Rep. Prog. Phys.* **79**, 016502 (2015).
- [88] M. Baggioli, M. Vasin, V. Brazhkin, and K. Trachenko, Gapped momentum states, *Phys. Rep.* **865**, 1 (2020), gapped momentum states.
- [89] G. Ruben, *Vortex and texture defects in radiation and matter wavefields*, Ph.D. thesis, Monash University (2010).